

---

# CLASSIFICATION AND MAPPING OF LOW-STATURED 'SHRUBLAND' COVER TYPES IN POST-AGRICULTURAL LANDSCAPES OF THE US NORTHEAST

---

A PREPRINT

## Michael J. Mahoney

Graduate Program in Environmental Science

State University of New York College of Environmental Science and Forestry  
Syracuse, New York, 13210  
mjmahone@esf.edu

## Lucas K. Johnson

Graduate Program in Environmental Science

State University of New York College of Environmental Science and Forestry  
Syracuse, New York, 13210  
ljohns11@esf.edu

## Colin M. Beier

Department of Sustainable Resources Management

State University of New York College of Environmental Science and Forestry  
Syracuse, New York, 13210  
cbeier@esf.edu

May 11, 2022

## Abstract

**Context:** Novel plant communities reshape landscapes and pose challenges for land cover classification and mapping that can constrain research and stewardship efforts. In the US Northeast, emergence of low-statured woody vegetation, or 'shrublands,' instead of secondary forests in post-agricultural landscapes is well-documented by field studies, but poorly understood from a landscape perspective, which limits the ability to systematically study and manage these lands.

**Objectives:** To address gaps in classification/mapping of low-statured cover types where they have been historically rare, we developed models to predict 'shrubland' distributions at 30m resolution across New York State (NYS), using machine learning and model ensembling techniques to integrate remote sensing of structural (airborne LIDAR) and optical (satellite imagery) properties of vegetation cover. We first classified a 1m canopy height model (CHM), derived from a "patchwork" of available LIDAR coverages, to define shrubland presence/absence. Next, these non-contiguous maps were used to train a model ensemble based on temporally-segmented imagery to predict 'shrubland' probability for the entire study landscape (NYS).

**Results:** Approximately 2.5% of the CHM coverage area was classified as shrubland. Models using Landsat predictors trained on the classified CHM were effective at identifying shrubland (test set AUC=0.893, real-world AUC=0.904), in discriminating between shrub/young forest and other cover classes, and produced qualitatively sensible maps, even when extending beyond the original training data.

**Conclusions:** After ground-truthing, we expect these shrubland maps and models will have

many research and stewardship applications including wildlife conservation, invasive species mitigation and natural climate solutions. Overall our results compared favorably in terms of accuracy with existing LULC products, suggesting that incorporation of airborne LiDAR, even from a discontinuous patchwork of coverages, can improve LULC classification of historically rare but increasingly prevalent ‘shrubland’ habitats across broader areas.

**Keywords** LiDAR · Landsat · shrubland · land cover · machine learning · remote sensing

## 1 Introduction

Human land use has fundamentally altered vegetation-environment relationships and created legacies that include the emergence of novel communities and ecosystem types (Foster et al. 1998, Cramer et al. 2008). In post-agricultural landscapes of eastern North America, these legacies include loss of plant diversity (Flinn and Vellend 2005) and widespread homogenization of vegetation composition and structure, relative to historical reconstructions (Foster et al. 1998, Flinn et al. 2005). Widespread abandonment of crop, pasture and industrial lands from the late-19th to middle-20th centuries created an expanding land base for invasion and emergence of novel communities (Williams and Jackson 2007, Fridley 2012, Alexander et al. 2015), with variable outcomes depending on prior land use practices (Stover and Marks 1998, Benjamin et al. 2005, Kulmatiski et al. 2006). Entirely novel communities have emerged in old-fields due to colonization by non-native plants, including invasive woody shrubs, which are much more likely to establish and become dominant in post-agricultural Cramer et al. (2008) and post-industrial sites (Spiering 2019) compared to closed-canopy forests of any successional age. Meanwhile, secondary forests across the US Northeast, including those established in old fields, lack sufficient advance regeneration to maintain productivity and resilience to changing disturbance regimes (Dey et al. 2019).

Among the outcomes of these changes, the emergence of low-statured vegetation or ‘shrublands’ as a more common cover type in the US Northeast has been suggested by numerous field studies, but is poorly understood from a landscape perspective. Here the term ‘shrubland’ reflects a physiognomic definition following King and Schlossberg (2014), which encompasses several types of plant communities found in the US Northeast, including: 1) young, regenerating or otherwise low-statured closed-canopy forests; 2) wetlands dominated by native shrubs (e.g., *Alnus* spp) or small-statured trees (e.g., *Picea mariana* in boreal peatlands); 3) uplands dominated by native shrubs (e.g., *Cornus racemosa*); and most recently, 4) upland shrub/scrub dominated by invasive woody (e.g., *Rhamnus* and *Lonicera* spp) and herbaceous (e.g., *Solidago* spp) perennials. Among the types above, regenerating forests and invasive shrub/scrub communities are of growing interest for research and management purposes, given their anthropogenic origins, their potential novelty in terms of composition and dynamics, and their implications for biodiversity and ecosystem services (Cramer et al. 2008, Hobbs et al. 2009, Perring et al. 2013, Dey et al. 2019). Despite their conservation value as wildlife habitat, especially for songbirds, shrublands are widely “unpopular” cover types in terms of their perceived aesthetic, recreational and economic values (Askins 2001, King and Schlossberg 2014). Although long disregarded, these lands are rapidly gaining attention in today’s urgent push to implement ‘natural climate solutions’ (Fargione et al. 2018) and identify ‘marginal’ or ‘underutilized’ lands for renewable energy generation.

However, current limitations to the classification and mapping of these cover types pose obstacles to advancing both science and stewardship opportunities (Hobbs et al. 2009). Shrublands are a very challenging cover class to identify from imagery alone, given the breadth of community types included (as noted above) and the high variability in density and canopy cover that exists within and among those community types (King and Schlossberg 2014). In practical terms this means that, when relying solely on imagery, shrublands encompass a full gradient from resembling herbaceous or barren land to resembling closed-canopy conditions (Brown et al. 2020). As a result, imagery-based approaches tend to classify shrubland categories with substantially lower accuracy than other LULC classes (Brown et al. 2020, Wickham et al. 2021).

A solution for this problem might be to incorporate additional, non-imagery sources of remote sensing data into LULC classification methodologies. LiDAR data collected through airborne laser scanning can provide essential information for identifying low-statured vegetation such as early-successional forests (Falkowski et al. 2009). In combination with imagery, LiDAR data can enable continuous, broad-scale estimation of canopy heights and other structural traits which greatly simplifies the task of distinguishing between low-statured and taller closed-canopy cover types (Ruiz et al. 2018). Unfortunately, the cost and logistical challenges of airborne LiDAR collection have constrained its availability to smaller extents and with much longer return intervals than provided by satellite imagery. Yet if canopy structural estimates from airborne LiDAR could be used to label a training dataset in order to fit models using satellite imagery, it should be possible to

produce models capable of identifying shrubland with greater accuracy than those trained on imagery alone, while being able to map/model a larger and more contiguous spatial extent than models relying on airborne LiDAR data as predictors.

Here we explored this approach to map shrubland across New York State (NYS), a largely post-agricultural landscape containing extensive old-fields populated mostly by secondary forests or invasive shrub/scrub communities, which are difficult to parse based on imagery alone. We leveraged a non-contiguous ‘patchwork’ of existing large-footprint LIDAR data sets by creating very high resolution (1 m) canopy height models that covered approximately 60% of the study area (NYS). By sampling from these canopy height maps, we trained machine learning models with temporally segmented Landsat imagery and LULC data products, and created a stacked ensemble to map the probability of shrubland at a high resolution (30 m) across the study area. Models were evaluated across multiple sensitivity/specificity thresholds to generate a range of map outputs that can support future ground-truthing efforts as part of research and stewardship activities. We provide new maps of ‘marginal’ cover types, such as invasive shrublands and degraded young forests, and demonstrate how to leverage an information-rich but geographically incomplete data source (LIDAR) for large-scale contiguous LULC classification and mapping based on widely available and standardized time-series imagery.

## 2 Methods

In order to map potential shrubland across New York State, we first identified low-stature vegetation across a discontinuous temporal patchwork of 1m resolution canopy height models (CHMs) derived from 19 distinct LiDAR point clouds. We then aggregated these 1m identifications into a 30m resolution raster surface, associated this surface with multiple data products derived from temporally matching remote sensing observations (including Landsat imagery as well as climate and topographic data), and used this data to produce a stacked ensemble model composed of three machine learning models combined through a logistic regression. We used this ensemble model to predict shrubland for a spatiotemporal patchwork matching LiDAR acquisitions, as well as for the entire state in 2019. A flowchart of this process is included as Figure 1.

### 2.1 Study area

New York State spans an area of 141,297 km<sup>2</sup> of the northeastern United States. Extensive land clearing for agriculture and industry in the 18th through 19th centuries decimated forests throughout the region, with forest cover dropping to 10-30% of the landscape by 1880 (Lorimer 2001). While total forest cover recovered rapidly at the turn of the 20th century, these forests were almost entirely young due to the combination of regeneration on abandoned farmland with the continual coppicing and harvesting of more established woodlots for fuelwood and other products (Whitney 1994). A variety of factors, among them a decrease in the use of wood for residential heating and an increase in forest conservation efforts, caused these forests to begin to mature in the 1930s, with the effect that the majority of forest stands across the Northeast are now over 100 years old. Two forest preserves, the Adirondack Park in the northeast and the Catskill Park in the southeast, have been protected in the New York State constitution as “forever wild”; timber harvesting has been generally prohibited on state-owned parcels in these regions since they were incorporated into the Forest Preserve, a process beginning in 1885. As a result, there is very little shrubland in these preserves.

Elevations across New York State range from -2 m to 1,584 m above sea level (U.S. Geological Survey 2019), with daily temperatures in 2019 ranging from -17 °C to 28 °C and monthly precipitation for the same period ranging from 5.0 cm to 16.8 cm (NOAA National Centers for Environmental Information 2022). The majority of the state occupies the northern hardwoods-hemlock forest region, though there are important inclusions of beech-maple-basswood and Appalachian oak communities in the western and southern reaches of the state, respectively (Dyer 2006).

### 2.2 LiDAR Data and Shrubland Identification

Although a distinction exists between “early-successional” and “young forest” habitats in eastern North America, for simplicity we have followed King and Schlossberg (2014) in combining these categories into a single ‘shrubland’ classification due to their structural similarity. This terminology aligns with Anderson (1976), who described shrubland in the eastern United States as “former croplands or pasture lands (cleared from original forest land) which now have grown up in brush in transition back to forest land to the extent that they are no longer identifiable as cropland or pasture from remote sensor imagery.”

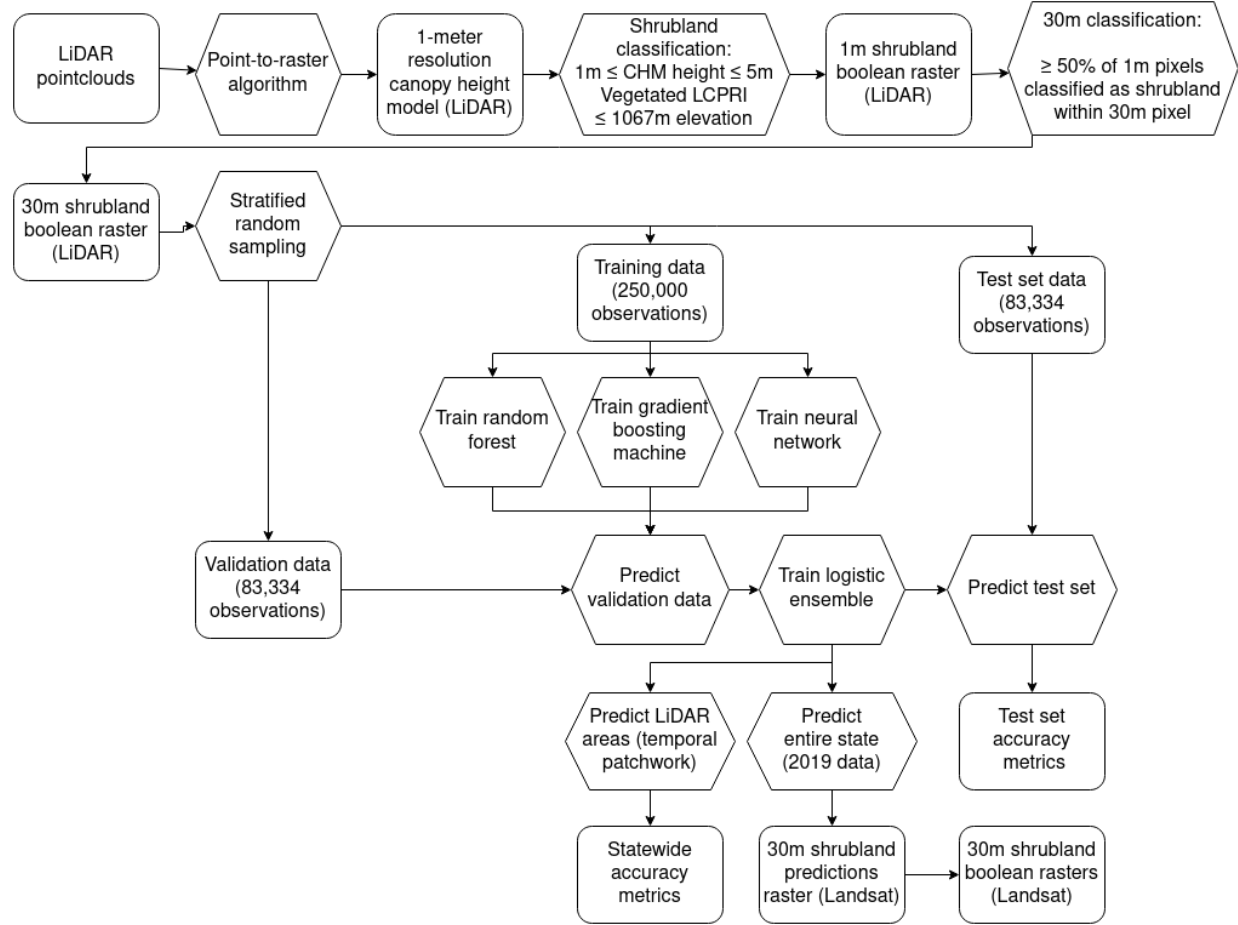


Figure 1: A flowchart diagram showing the key elements of the identification methodology. Rectangular boxes represent data products and results, while hexagonal boxes represent methodological steps.

Shrubland was identified using 19 distinct leaf-off LiDAR point clouds coverages, collected between 2014 and 2020 (Figure 2). More information about individual LiDAR coverages is available as Online Resource 1. These point clouds were converted to 1 m canopy height models (CHMs) using a point-to-raster algorithm implemented in the lidR R package (Roussel et al. 2020). These CHMs were then masked to exclude any pixel assigned a non-vegetation primary land cover classification by the temporally-matching USGS LCMAP land cover product (namely the developed, water, ice and snow, and barren classes) using the “terra” R package (Brown et al. 2020, Hijmans 2021, R Core Team 2021). CHMs were also masked to exclude any pixel with an elevation above 1067m (3500 ft), as shorter canopy heights at these elevations likely represent krumholz (stunted trees near elevational treeline) instead of shrubs or regenerating forest. Shrubland was then defined as any 1 m pixel with a CHM height between 1-5 m. The lower threshold was defined to avoid classifying cropland and human structures (such as low walls) as shrubland, and the upper threshold defined to match the USGS NLCD definition of shrubland, which was derived from the Anderson classification system (Anderson et al. 1976, Yang et al. 2018). These 1 m pixels were then aggregated into 30 m resolution pixels using GDAL (GDAL/OGR contributors 2021), with each 30 m pixel defined as shrubland if more than 50% of its constituent 1 m subpixels were identified as shrubland.

### 2.3 Predictor Creation

We produced a set of 10 annual Landsat-derived predictors by processing Landsat analysis ready data (ARD) in Google Earth Engine (GEE) (Gorelick et al. 2017, Dwyer et al. 2018), using the Landtrendr implementation in GEE (hereafter LT-GEE). Processing of Landsat ARD using LT-GEE was done to fill gaps (e.g., clouds

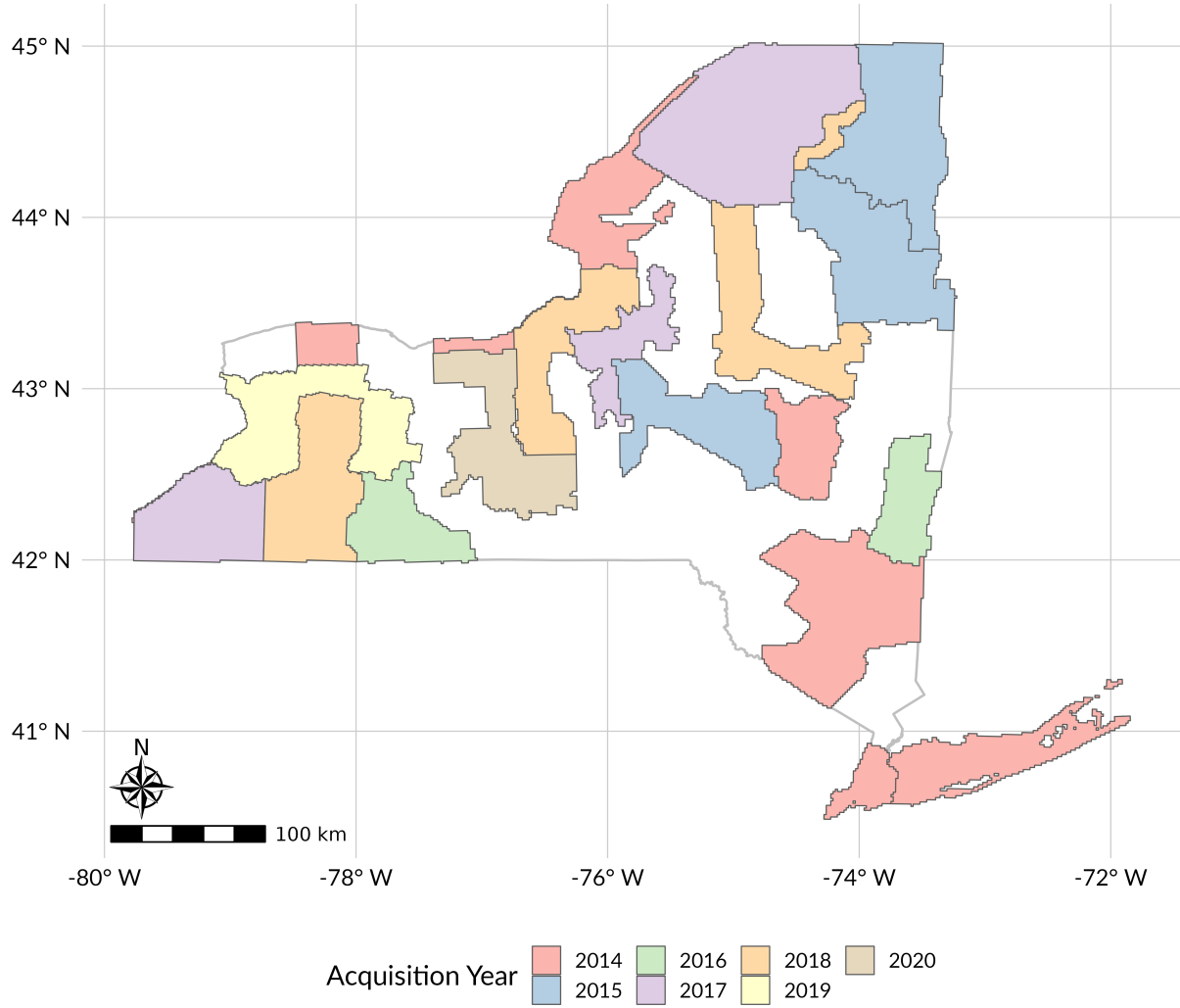


Figure 2: Boundaries for all LiDAR coverages used in this project, colored by year of data acquisition. More information about each coverage is included as Online Resource 1.

and shadows) in the annual time series, smooth interannual variations (noise), and quantify the disturbance history for each pixel (Kennedy et al. 2010, 2018). The LT-GEE predictors included three tasseled cap indices, (brightness - TCB, greenness - TCG, and wetness - TCW) and their respective deltas computed with a 1-year lag, all fit to Normalized Burn Ratio (NBR) temporally segmented vertices, as well as an NBR index and respective 1-year delta (Kauth and Thomas 1976, Cocke et al. 2005, Kennedy et al. 2018). We also processed a separate NBR segmented time-series with LT-GEE parameters tailored to be more sensitive to the timing of discrete disturbances using LT-GEE code to produce two predictors describing disturbances at an individual pixel: year-of-most-recent-disturbance (YOD; 1985-2020) and associated magnitude-of-most-recent-disturbance (MAG; unitless measure of change in NBR value) (Kennedy et al. 2018). The 8 annual indices and associated deltas aimed to capture the surface reflectance for a given pixel at a given time, while the two disturbance predictors aimed to describe disturbance history for a given pixel. NBR was chosen as the base predictor, providing disturbance history information and temporal break-points to which tasseled cap predictors were fit, as it has been shown to be the most sensitive for capturing disturbance events (Kennedy et al. 2010). Information on LT-GEE parameters used is included as Online Resource 2.

In addition to Landsat-derived predictors, a set of “steady-state” ancillary predictors was included to represent geospatial variation in climate and topography (Kennedy et al. 2018). These predictors included precipitation and temperature 30 year normals derived from PRISM Climate Group data (PRISM Climate Group 2022),

Table 1: Definitions of predictors used for model fitting.

Predictor	Definition
TCB, TCW, TCG	Tassled cap brightness, wetness, and greenness, with noise removed using LT-GEE
NBR	Normalized burn ratio with noise removed using LT-GEE
MAG, YOD	Magnitude and year of most recent disturbance, as identified using LT-GEE
PRECIP, TMAX, TMIN	30-year normals for precipitation, maximum temperature, and minimum temperature, derived from annual PRISM climate models
ASPECT, ELEVATION, SLOPE, TWI	Aspect, elevation, slope, and topographic wetness index derived from a 30-meter digital elevation model
LCSEC	LCMAP secondary land cover classification

the secondary land cover classification prediction from LCMAP (Brown et al. 2020), and elevation, aspect, slope, and topographic wetness indices derived from a 30 meter digital elevation model (Beven and Kirkby 1979, U.S. Geological Survey 2019, Mahoney et al. 2022). In total, models were fit using 14 separate predictors (Table 1).

## 2.4 Model Fitting and Evaluation

Each LiDAR-derived shrubland layer was combined with a set of temporally matching predictors, which were then merged into a single “temporal patchwork” data set representing each region of the state during its year of LiDAR acquisition. A total of 416,668 pixels were then sampled from this patchwork set, stratified so that half (208,334) represented shrubland and half other land cover types. These pixels were then split at random into a training set of 250,000 pixels, a validation set of 83,334 pixels, and a hold-out evaluation set of 83,334 pixels. We then fit three separate models, a random forest (Breiman 2001), stochastic gradient boosting machine (Friedman 2002), and deep neural network (LeCun et al. 2015), against the training data set to estimate the probability of a given pixel representing shrubland. Models were fit using hyperparameters chosen to minimize out-of-sample binary cross entropy (Good 1952); more information about the final models used is included as Online Resource 3. We then used each of these models to predict the probability of a pixel representing shrubland for each observation in the validation data set. Next, we fit a logistic regression to the validation set predictors and predicted probabilities to combine our three models into a single stacked ensemble model (Wolpert 1992, Dormann et al. 2018). This ensemble model was then used to generate predictions for the test set, for the temporal patchwork data set, and for data reflecting the entire state for 2019 (chosen in order to compare predictions to the 2019 NLCD land cover map). The same model was used for predicting each of these data sets.

Probability thresholds used to classify individual pixels were chosen using model predictions for the validation set. Four separate thresholds were identified: the one that maximized the model’s summed sensitivity (Equation 1) and specificity (Equation 2), calculated using Youden’s J statistic (hereafter “Youden Optimal”) (Youden 1950); and three that maximized sensitivity while keeping specificity above 90%, 95%, and 99%. All metrics were calculated considering shrubland pixels as “positive” cases; higher specificity targets reflected the relatively rare abundance of shrubland throughout the state (approximately 2.5% of mapped pixels) necessitating low levels of false positives. Predictions against both the test set and the temporal patchwork data set were classified using each of these thresholds, then assessed using sensitivity (Equation 1), specificity (Equation 2), precision (Equation 3), and F1 score (Equation 4).

$$\text{Sensitivity} = \frac{TP}{TP + FN} \quad (1)$$

$$\text{Specificity} = \frac{TN}{FP + TN} \quad (2)$$

$$\text{Precision} = \frac{TP}{TP + FP} \quad (3)$$

$$F1 = \frac{2 * Precision * Sensitivity}{Precision + Sensitivity} \quad (4)$$

Where  $TP$  is the number of pixels correctly classified as shrubland,  $FP$  the number of pixels incorrectly classified as shrubland,  $TN$  the number of pixels correctly classified as not being shrubland, and  $FN$  the number of pixels incorrectly classified as not being shrubland.

Models were additionally assessed using the area under the receiver operating characteristic curve (AUC) (Austin and Steyerberg 2012), calculated for the test set using all observations and for the temporal patchwork set using a random sample of 1,000,000 pixels due to computational limitations. Given the imbalance of our classes, we do not report overall accuracy or balanced accuracy for either the test set or the temporal patchwork, given that approximately 97.5% overall accuracy could be achieved by never predicting shrubland.

All models were fit using either R version 4.1.2 (R Core Team 2021) or Python version 3.9.10 (Python Core Team 2022). Random forests were fit using the “ranger” R package (Wright and Ziegler 2017), gradient boosting machines using “lightgbm” (Ke et al. 2017), and neural nets using “keras” (Chollet 2015).

### 3 Results

#### 3.1 LiDAR Classification

Based on LiDAR-derived CHMs, approximately 2.5% of the study area was initially mapped as shrubland (1-5 m tall), representing about  $1.83 \times 10^6$  ha of the  $73.3 \times 10^6$  ha land area that remained after LCMAP masking removed non-vegetated cover types (Figure 4). Shrubland was identified in every LiDAR coverage, with proportions ranging from 0.3% (Great Gully) to 7.6% (Great Lakes) of the coverage footprint area (Figure 3).

Shrubland cover was present in each vegetated LCMAP primary classification classes, but was weighted more heavily towards areas classified as cropland or tree cover (Table 2). Approximately 7.3% of land classified by LCMAP as “grassland/shrub” was classified as shrubland through this process, though this result should not be over-interpreted given the LCMAP “grassland/shrub” category includes herbaceous land covers alongside shrublands (Brown et al. 2020).

#### 3.2 Model Accuracy

Model accuracy assessments focused on the logistic ensemble model, which combined the three component machine learning methods into a single prediction. Accuracy assessments for the component models are included as Online Resource 4.

Our model was highly effective at distinguishing between shrubland pixels and other cover types, with an AUC of 0.893 against the test set and 0.904 against a random sample of  $1 \times 10^6$  pixels from the LiDAR temporal patchwork data set (Figure 4). When evaluating models against the balanced test set, the highest F1 score (0.816) was achieved using the Youden-optimal classification threshold (Table 3). The model retained its high AUC, sensitivity, and specificity when predicting the LiDAR temporal patchwork data set, precision was lower due to the large imbalance between shrubland and other cover classes across the state. As a result, the model attained its highest F1 score of 0.307 when using a classification threshold to that targeted 95% specificity.

##### 3.2.1 LiDAR Patchwork Predictions

When predicting the temporal patchwork, our model predicted the highest probabilities of shrubland along the northern reaches of the state, matching the distribution of shrubland in the “true” LiDAR-derived surface (Figure 5). However, the model also predicted higher than average probabilities of shrubland in the southwestern and central regions of the state, neither of which were reflected in the original LiDAR-derived surface.

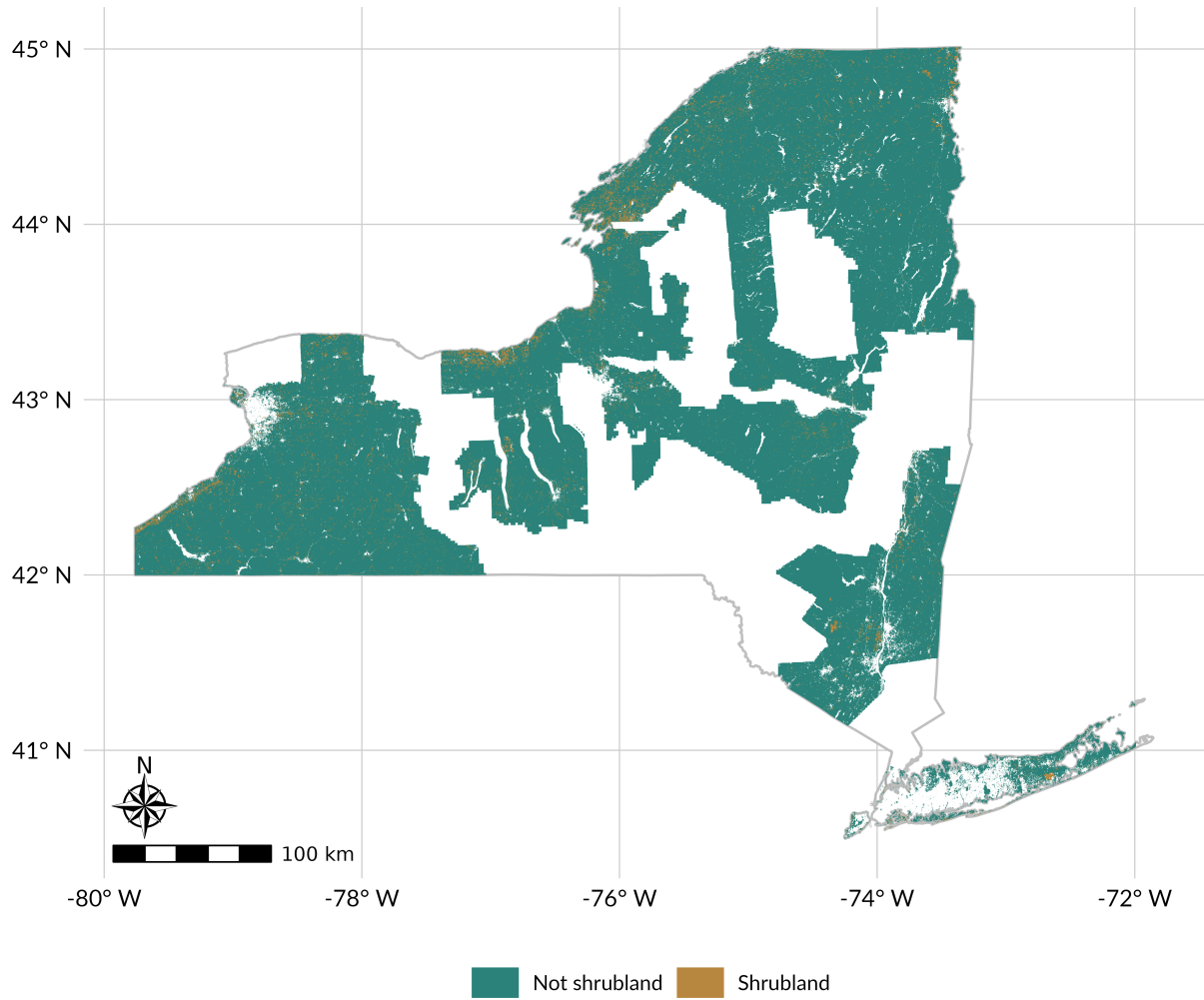


Figure 3: Identified shrubland areas within each available LiDAR coverage. Shrubland was defined at a 1 meter resolution as being any area within a vegetated LCPRI land cover class and below 1067 meters elevation with a LiDAR-derived height between 1 and 5 meters. 30 meter pixels, used for analysis and modeling, were then defined as shrubland if more than 50% of their contained 1 meter pixels were classified as shrubland. In total, approximately 2.5% of 30 meter pixels were classified as shrubland.

Table 2: Total area and amount of shrubland within each LCMAP primary classification, in square kilometers. Both the temporal patchwork and statewide models were classified using a 95% specificity threshold.

LCMAP primary classification	Total area	Shrubland area	% Shrubland
<b>LiDAR Classification</b>			
Cropland	20 077.6	679.5	3.4%
Grass/Shrub	2 085.3	151.8	7.3%
Tree Cover	44 879.5	597.2	1.3%
Wetland	6 635.0	467.9	7.1%
<b>Temporal Patchwork</b>			
Cropland	20 077.6	1 451.2	7.2%
Grass/Shrub	2 085.3	416.2	20.0%
Tree Cover	44 879.5	1 428.3	3.2%
Wetland	6 635.0	1 166.3	17.6%
<b>2019 Statewide</b>			
Cropland	29 922.9	2 005.9	6.7%
Grass/Shrub	2 994.2	549.3	18.3%
Tree Cover	69 419.0	1 694.6	2.4%
Wetland	9 008.3	1 425.0	15.8%

Table 3: Model accuracy metrics for logistic ensemble model with predictions classified using various thresholds, calculated using both the balanced test set and the LiDAR patchwork surface. AUC for the LiDAR patchwork was calculated using a random sample of 1,000,000 pixels, while all other metrics used all predicted pixels. Thresholds were selected using a separate validation set, using values chosen to maximize the Youden J statistic ("Youden optimal") or to target a certain minimum specificity ("% specificity").

	Threshold	Sensitivity	Specificity	Precision	F1
<b>Test set (AUC: 0.893)</b>					
Youden optimal	0.489	0.842	0.780	0.791	0.816
90% specificity	0.755	0.659	0.900	0.867	0.807
95% specificity	0.840	0.496	0.949	0.906	0.641
99% specificity	0.907	0.218	0.989	0.952	0.355
<b>LiDAR patchwork (AUC: 0.904)</b>					
Youden optimal	0.489	0.858	0.783	0.094	0.169
90% specificity	0.755	0.689	0.896	0.149	0.245
95% specificity	0.840	0.514	0.951	0.219	0.307
99% specificity	0.907	0.247	0.989	0.376	0.298

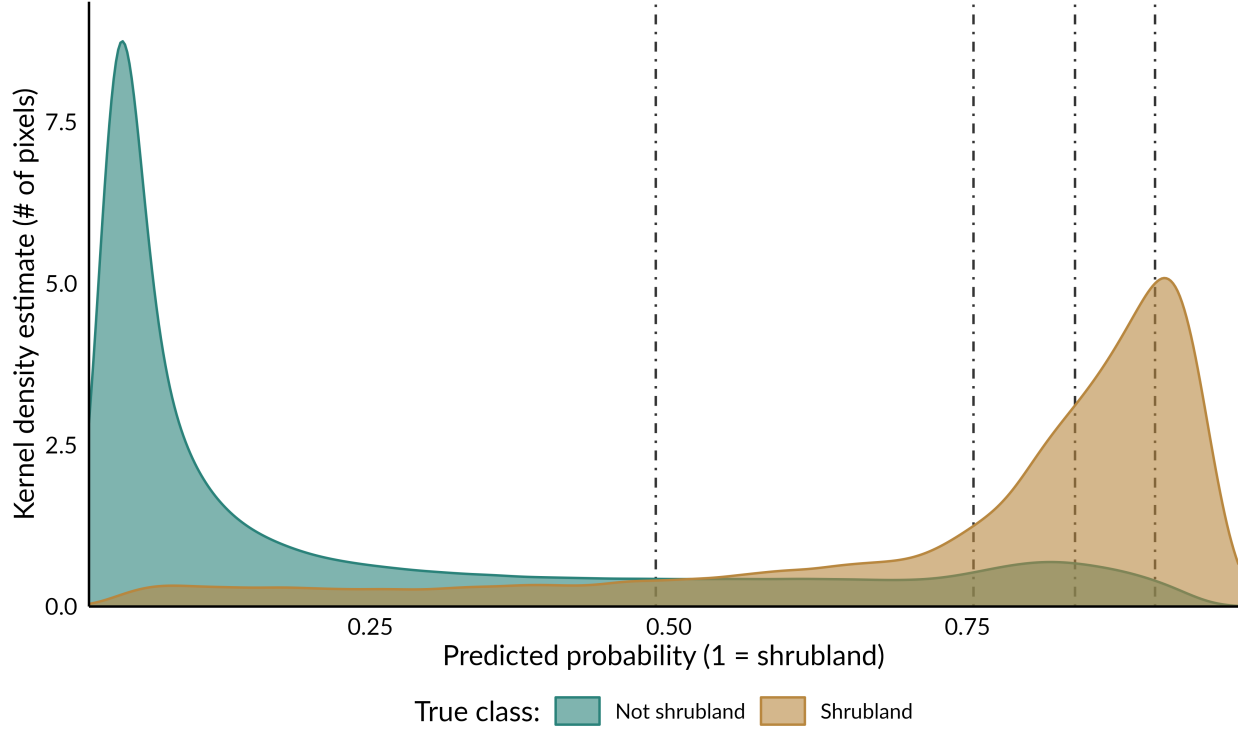


Figure 4: Smoothed kernel density estimates of predicted probability of shrubland for both shrubland and non-shrubland pixels, calculated using a random sample of 1,000,000 pixels taken from the LiDAR patchwork prediction surface using the logistic ensemble model. Vertical lines indicate each of the four probability thresholds used to classify pixels. Colors represent the correct classification of the pixel.

Boolean surfaces classified using the Youden optimal probability threshold classified 23% of pixels as shrubland, an order of magnitude greater than the 2.5% identified from the “true” LiDAR-derived surface (Figure 6). More conservative predictions based on specificity thresholds predicted a lower proportion of shrubland (90% specificity: 11.9%; 95% specificity: 6.1%, 99% specificity: 1.7%) with a higher precision, resulting in more accurate overall predictions and higher F1 scores.

### 3.2.2 2019 Statewide Predictions

Model predictions reflected a similar geographical distribution of shrubland when extrapolating beyond the spatiotemporal boundaries of available LiDAR data to map shrubland across the entire state for 2019. Areas throughout the Adirondack Park and the Catskill Park, montane regions with mostly contiguous forest cover, showed notably less shrubland than more heavily populated areas (Figure 7). As expected, predictions in areas included in the LiDAR patchwork data set resembled the predictions for the LiDAR patchwork surface (Figure 5), though with some variation due in part to the temporal mismatch.

Shrubland probabilities were highest in areas classified by 2019 LCMAP as shrubland, as well as in areas classified as wetlands by either LCMAP or NLCD (Figure 8). Areas classified as tree cover were assigned extremely low probabilities.

Predictions for 2019 classified using the Youden optimal probability threshold classified 22.3% of the state as shrubland (Figure 9), in line with the Youden optimal classified LiDAR patchwork data set. The target-specificity thresholds classified more realistic proportions (90% specificity: 10.7%; 95% specificity: 5.1%, 99% specificity: 1.2%).

A minority of predicted shrubland was located in wetland areas, as delineated by the US Fish and Wildlife Service (U.S. Fish and Wildlife Service 2021). The proportion of shrubland pixels in wetland areas increased

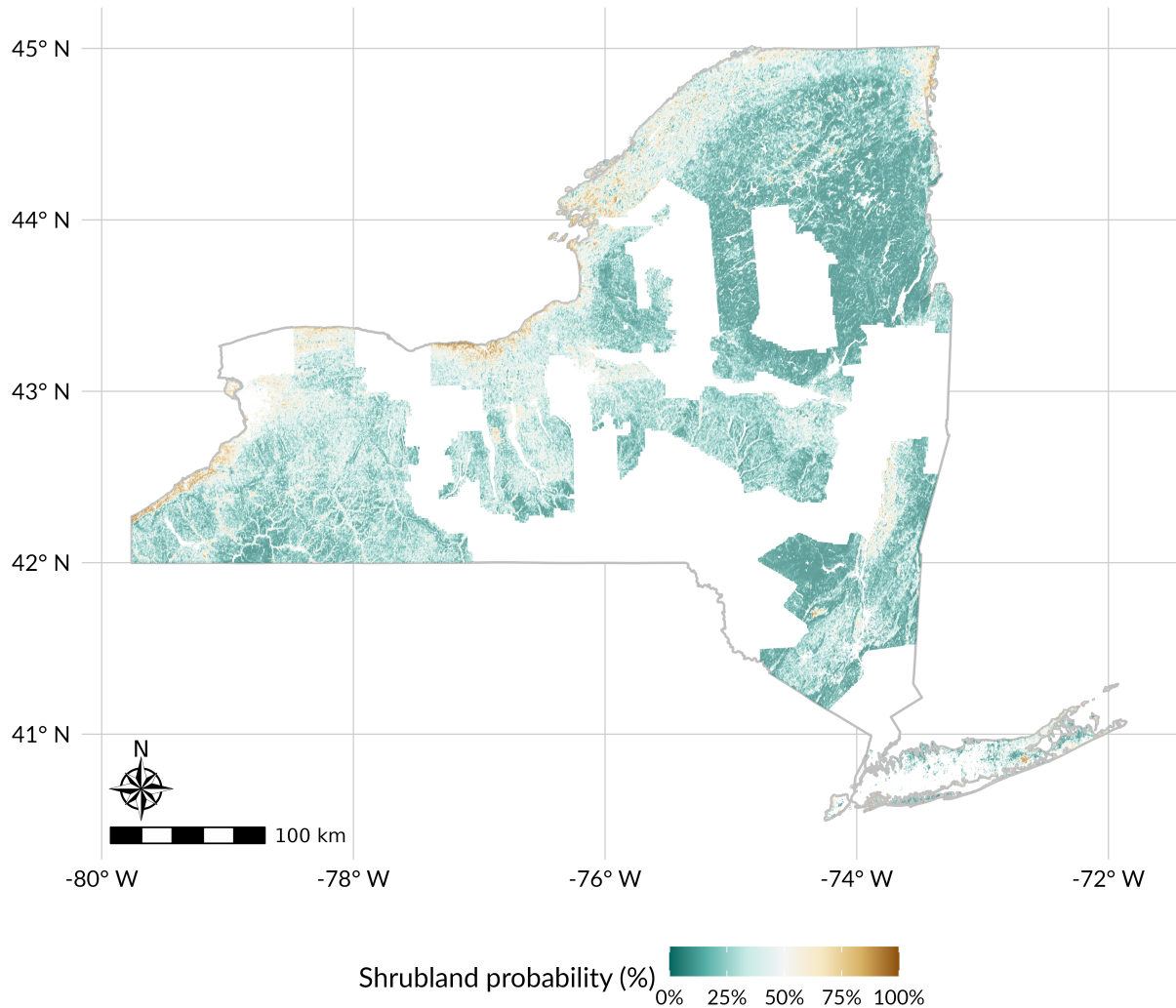


Figure 5: Predicted probability of shrubland for the boundaries of all used LiDAR coverages, from the logistic ensemble model. Predictions were made using data reflecting the same year as LiDAR acquisition; the map therefore represents a temporal patchwork of predictions. Pixels in non-vegetated LCPRI land cover classes (developed, water, ice/snow, and barren) or above 1067 meters in elevation were not mapped and are shown in white.

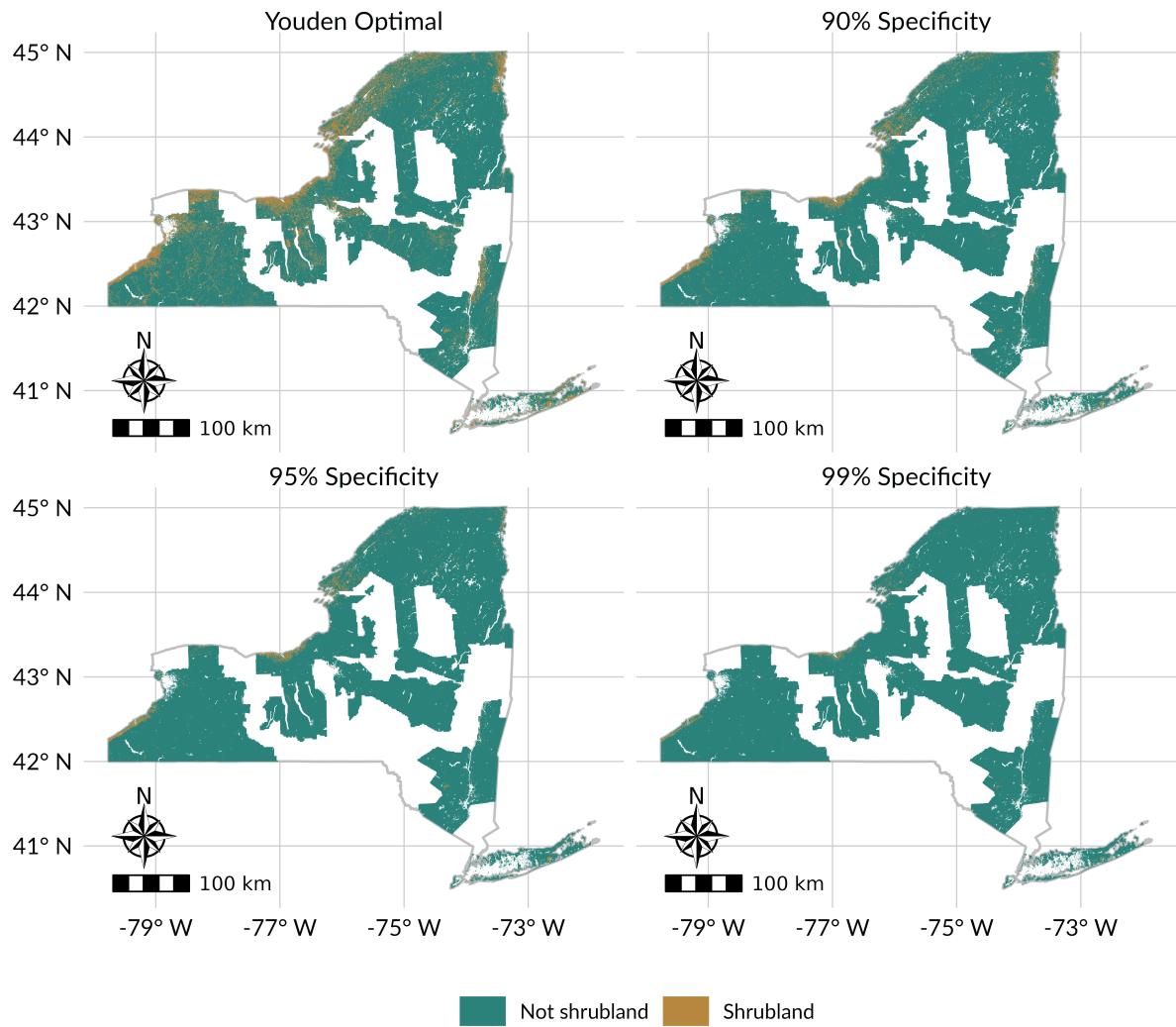


Figure 6: Predicted shrubland locations within each LiDAR coverage, from the logistic ensemble model. Predicted pixel probabilities were classified using either the Youden-optimal threshold (which maximizes both sensitivity and specificity) or a threshold chosen to target a certain level of specificity, using thresholds derived from the validation data set. Predictions were made using data reflecting the same year as LiDAR acquisition; the map therefore represents a temporal patchwork of predictions. Pixels in non-vegetated LCPRI land cover classes (developed, water, ice/snow, and barren) or above 1067 meters in elevation were not mapped and are shown in white.

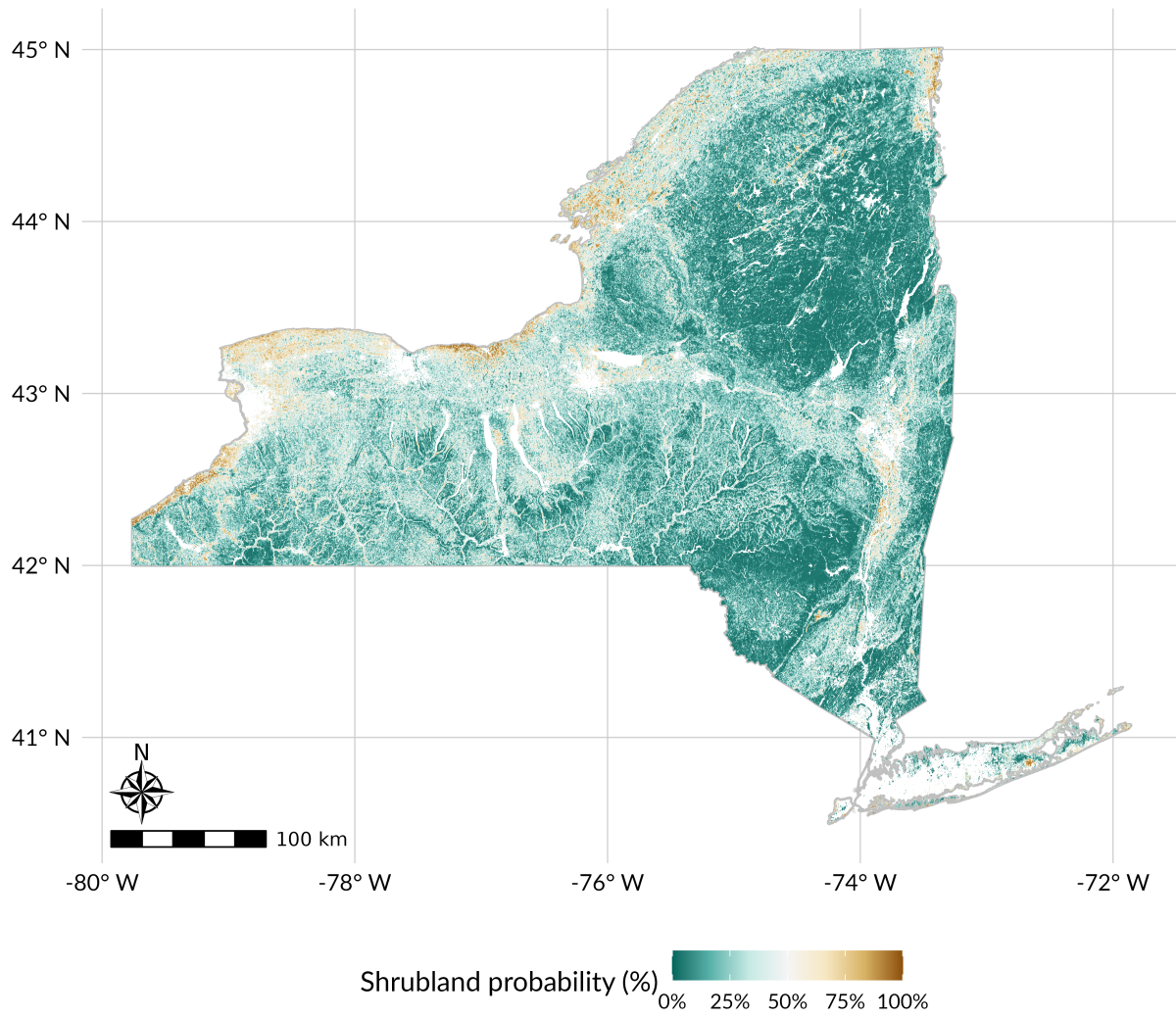


Figure 7: Predicted probability of shrubland for 2019 across all mapped areas within New York State, from the logistic ensemble model. Pixels in non-vegetated LCPRI land cover classes (developed, water, ice/snow, and barren) or above 1067 meters in elevation were not mapped and are shown in white.

with specificity thresholds, increasing from 16.27% at the Youden optimal threshold to 26.19% at the 99% specificity threshold (Figure 10).

#### 4 Discussion

In this study, we produced a model capable of predicting shrubland locations, as delineated using airborne LiDAR data and LCMAP LULC classifications, across a large, fragmented and heterogeneous landscape (New York State). Overall, we found that our models were effective at distinguishing between shrubland and other land cover classes, and produced qualitatively sensible map outputs, even when extrapolating beyond the original training data. Despite inherent challenges in modeling a rare cover type (~2% by area), our model accuracy for shrubland mapping improves on existing products such as LCMAP (Brown et al. 2020). Our results serve to demonstrate that incorporating airborne LiDAR data can improve LULC classifications, particularly for marginal, transitional and emergent cover types that may not be well represented in LULC class definitions. More practically, we provide new maps of ‘marginal’ cover types, such as invasive shrub/scrub and degraded young forests, that have emerged mostly on post-agricultural and post-industrial lands during the last century. While our model is not without its limitations, chiefly in the labeling of training data and

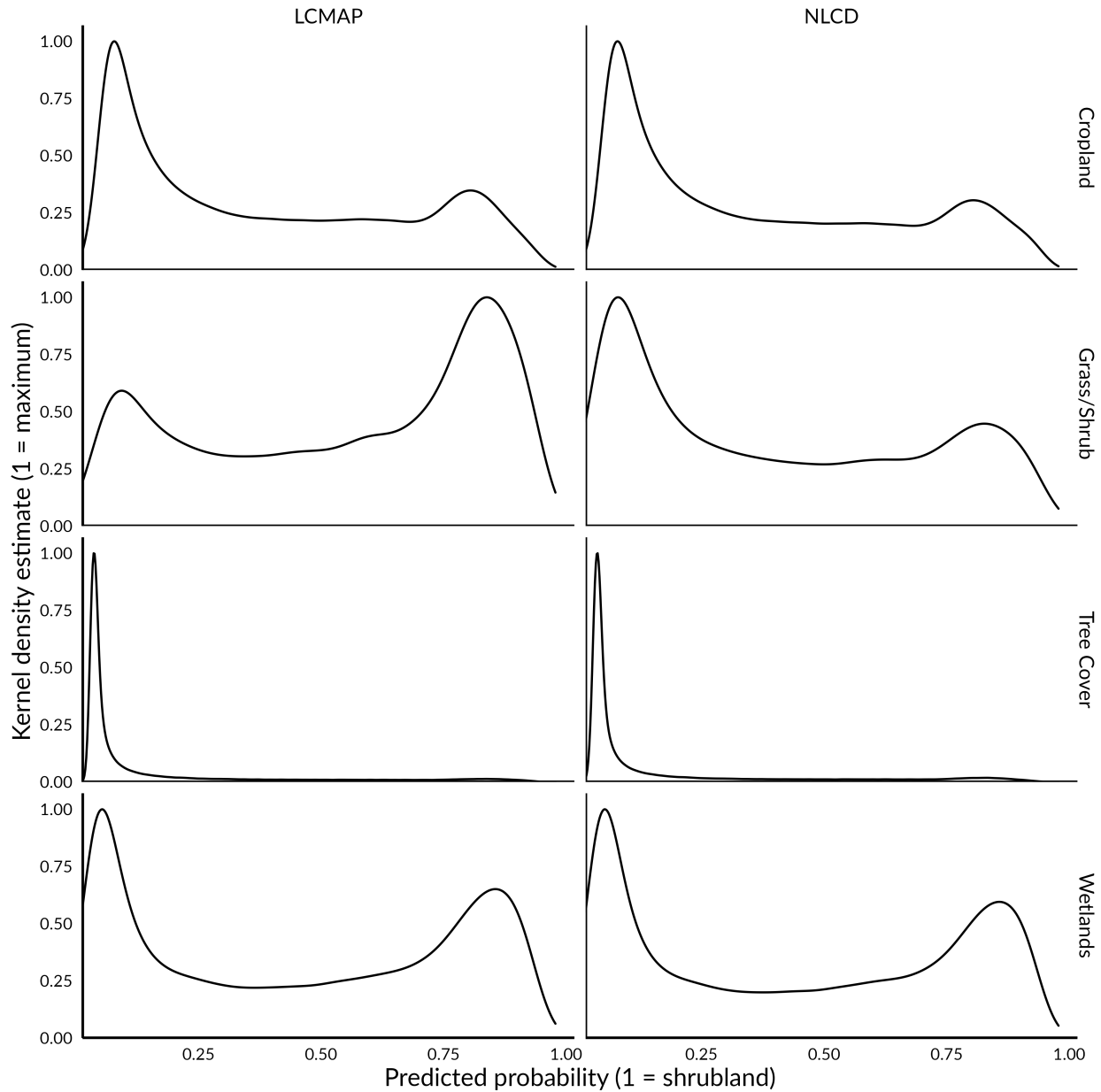


Figure 8: Smoothed kernel density estimates of predicted probability of shrubland for the included LCMAP classes, calculated using a random sample of 1,000,000 pixels taken from the LiDAR patchwork prediction surface using the logistic ensemble model. Density estimates have been rescaled so that the most common probability for each panel is assigned a value of 1. NLCD land cover classes were remapped to LCMAP classes using LCMAP-defined translations.

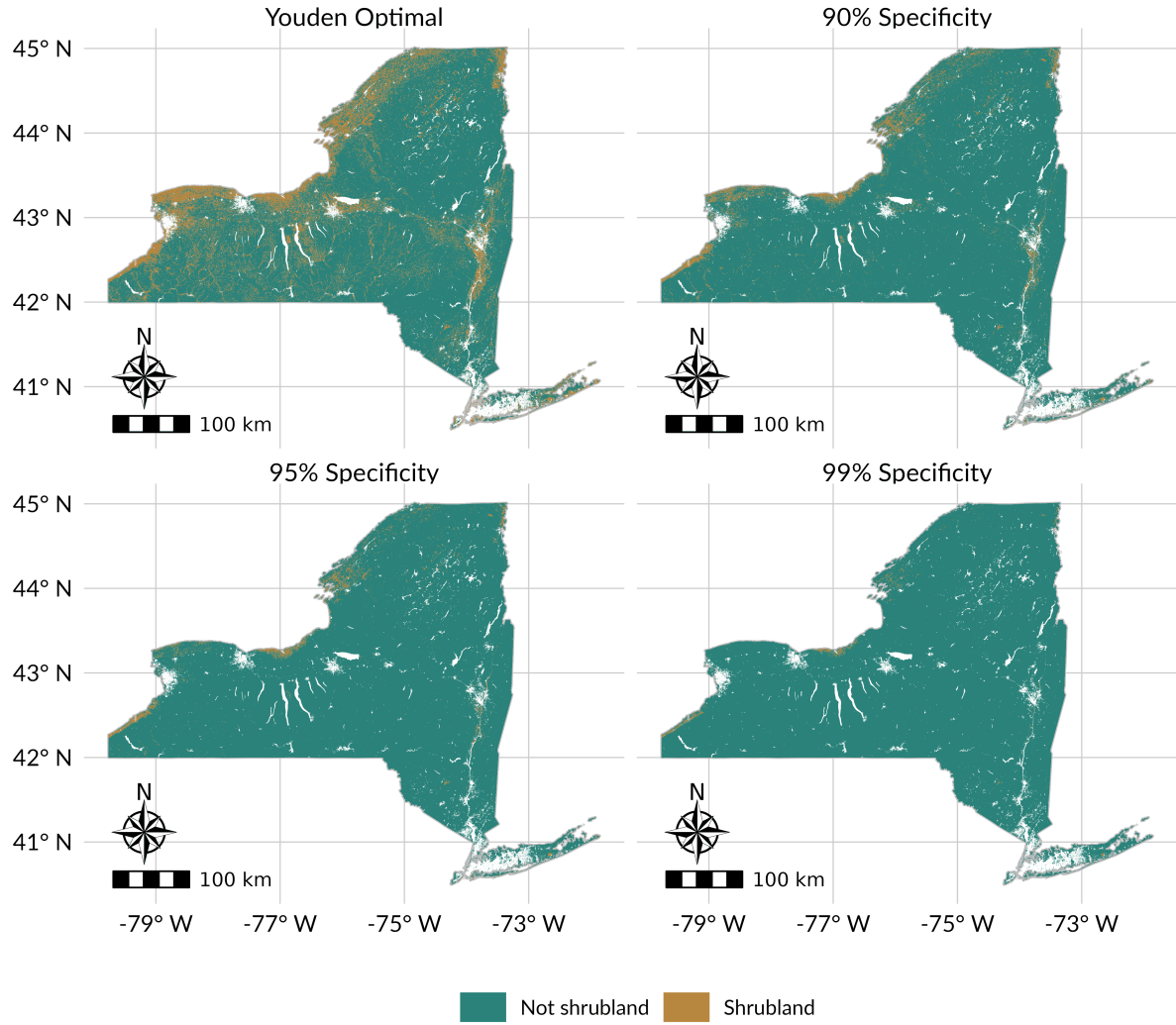


Figure 9: Predicted shrubland locations for 2019 across the entire state, from the logistic ensemble model. Predicted pixel probabilities were classified using either the Youden-optimal threshold (which maximizes both sensitivity and specificity) or a threshold chosen to target a certain level of specificity, using thresholds derived from the validation data set. Pixels in non-vegetated LCPRI land cover classes (developed, water, ice/snow, and barren) or above 1067 meters in elevation were not mapped and are shown in white.

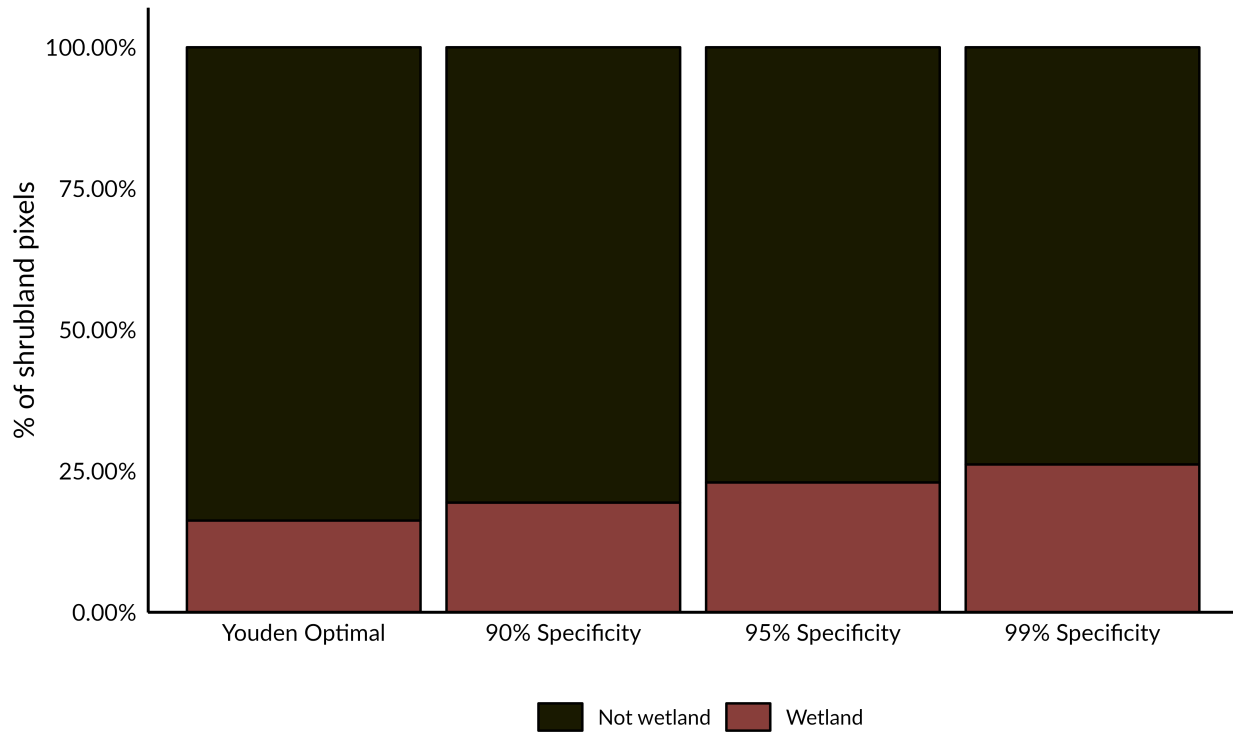


Figure 10: Percentage of predicted shrubland, from the statewide 2019 logistic ensemble model, located in wetlands delineated by the US Fish and Wildlife Service. A pixel was identified as being in wetlands if more than half of the pixel area was delineated as wetland.

in the inherent difficulty in predicting rare events, it was effective at distinguishing between shrubland and other cover types. This modeling approach addresses a persistent measurement gap and enables monitoring, research, and stewardship of these emerging and novel communities at a landscape scale.

#### 4.1 Model predictions reflect known patterns

Our model predictions, both for areas included in the LiDAR patchwork and for the 2019 surface, reflect known patterns in land use and land cover throughout New York State. Although areas classified as developed by LCMAP were excluded from predictions, areas of higher-intensity human land use – such as the Hudson Valley in the eastern region of the state, the I-90 highway corridor running East-West (along roughly 43N latitude), and the northern border of the state, particularly around the Great Lakes – were consistently classified as having a higher probability of shrubland (Figure 5, Figure 7). These areas have likely been more recently impacted by human activity, with cropland only more recently being left to natural regeneration. By the same pattern, areas of lower population density and less intensive land use history such as the Adirondack and Catskill Parks have consistently low probabilities of shrubland, reflecting the older, mid-successional forests that characterize these areas. When extrapolating beyond the spatiotemporal boundaries of available LiDAR data, our 2019 statewide model predicted a similar abundance of shrubland with a similar regional distribution as the LiDAR patchwork data set, with similar areas of shrubland along the Great Lakes and adjacent to human population centers. This pattern reflects the continuing decline in agricultural land across New York State (USDA National Agricultural Statistics Service 2019); while much agricultural land is being converted to developed land classes, a large proportion of former cultivated lands have also been allowed to regenerate.

#### 4.2 Predicting rare events is challenging

As previously noted, shrubland is rare in New York due to the state's history of deforestation and regeneration combined with the relatively mild disturbance regime of the northern forest (Lorimer 2001). One challenge in

predicting rare events is that even a low percentage of false positives can quickly drown out true positives; a model with 90% specificity predicting a data set with only 1% positive cases will produce 9 false positives for every true positive it generates.

For this reason, classified our predictions using a range of thresholds targeting increasingly high specificities (Table 3). These more stringent thresholds successfully increased model precision (sometimes referred to as “positive predictive power”), making it more likely that a positive prediction represents a true positive, though at the cost of lower sensitivity. Of these three thresholds, the 95% specificity target best balanced sensitivity and precision, based on its F1 score. Using this threshold, more than half of true shrubland pixels were correctly classified and 22% of positive predictions reflect true shrubland (as defined in the LiDAR analysis), approximately 10 times better than simply guessing using the shrubland occurrence rate of 2.5%. Although there is room for improvement, this level of accuracy is still sufficient to identify potential areas for further research and stewardship.

This work should be of interest to both those producing LULC models and products and those interested in the research and management of shrubland at a landscape level. For producers of LULC products, this work suggests that combinations of remote sensing data from multiple sources can improve model predictive accuracy, even if one source (such as airborne LiDAR in this study) is only used to improve the quality of training set labels. It also potentially speaks to the benefits of more targeted, regional LULC products to supplement the well-established national models; regional efforts that can take advantage of regional data sets to improve accuracy on cover types of regional importance.

## 5 Conclusion

This study aimed to predict the locations of shrubland across New York State, in order to improve both understanding and stewardship of these plant communities. Using a stacked ensemble model combining multiple machine learning models fit to data labeled using a combination of airborne LiDAR data and national LULC products, we generated predictions of shrubland occurrences for both all spatiotemporal extents with matching LiDAR data and for the entirety of New York State for 2019. Our model was highly effective at distinguishing between shrubland and other cover types on both the test set (AUC 0.893) and the LiDAR temporal patchwork (AUC 0.904), and balanced sensitivity and precision more effectively than a leading national LULC product (LCMAP). These results suggest that combining remote sensing data from multiple sources may improve LULC models, that regionally focused LULC models may complement national competitors, and that shrubland may be effectively identified and monitored using spaceborne remote sensing data.

## 6 Declarations

### 6.1 Funding

Funding was provided by the Environmental Protection Fund via the NYS Department of Environmental Conservation.

### 6.2 Competing interests

The authors have no relevant financial or non-financial interests to disclose.

## References

- Alexander, J. M. et al. 2015. Novel competitors shape species' responses to climate change. - *Nature* 525: 515–518.
- Anderson, J. R. et al. 1976. A land use and land cover classification system for use with remote sensor data. - US Government Printing Office.
- Askins, R. A. 2001. Sustaining biological diversity in early successional communities: The challenge of managing unpopular habitats. - *Wildlife Society Bulletin* 29: 407–412.
- Austin, P. C. and Steyerberg, E. W. 2012. Interpreting the concordance statistic of a logistic regression model: Relation to the variance and odds ratio of a continuous explanatory variable. - *BMC Medical Research Methodology* in press.
- Benjamin, K. et al. 2005. Vegetation composition and succession of abandoned farmland: Effects of ecological, historical and spatial factors. - *Landscape ecology* 20: 627–647.
- Beven, K. J. and Kirkby, M. J. 1979. A physically based, variable contributing area model of basin hydrology. - *Hydrological Sciences Bulletin* 24: 43–69.
- Breiman, L. 2001. Random Forests. - *Machine Learning* 45: 5–32.
- Brown, J. F. et al. 2020. Lessons learned implementing an operational continuous united states national land change monitoring capability: The land change monitoring, assessment, and projection (LCMAP) approach. - *Remote Sensing of Environment* 238: 111356.
- Chollet, F. 2015. Keras.
- Cocke, A. E. et al. 2005. Comparison of burn severity assessments using differenced normalized burn ratio and ground data. - *International Journal of Wildland Fire* 14: 189–198.
- Cramer, V. A. et al. 2008. What's new about old fields? Land abandonment and ecosystem assembly. - *Trends in ecology & evolution* 23: 104–112.
- Dey, D. C. et al. 2019. Barriers to natural regeneration in temperate forests across the USA. - *New Forests* 50: 11–40.
- Dormann, C. F. et al. 2018. Model averaging in ecology: A review of bayesian, information-theoretic, and tactical approaches for predictive inference. - *Ecological Monographs* 88: 485–504.
- Dwyer, J. L. et al. 2018. Analysis ready data: Enabling analysis of the landsat archive. - *Remote Sensing* in press.
- Dyer, J. M. 2006. Revisiting the deciduous forests of eastern north america. - *BioScience* 56: 341–352.
- Falkowski, M. J. et al. 2009. Characterizing forest succession with lidar data: An evaluation for the inland northwest, USA. - *Remote Sensing of Environment* 113: 946–956.
- Fargione, J. E. et al. 2018. Natural climate solutions for the united states. - *Science Advances* 4: eaat1869.
- Flinn, K. M. and Vellend, M. 2005. Recovery of forest plant communities in post-agricultural landscapes. - *Frontiers in Ecology and the Environment* 3: 243–250.
- Flinn, K. M. et al. 2005. Environmental causes and consequences of forest clearance and agricultural abandonment in central new york, USA. - *Journal of Biogeography* 32: 439–452.
- Foster, D. R. et al. 1998. Land-use history as long-term broad-scale disturbance: Regional forest dynamics in central new england. - *Ecosystems* 1: 96–119.
- Fridley, J. 2012. Extended leaf phenology and the autumn niche in deciduous forest invasions. - *Nature* 485: 359–362.
- Friedman, J. H. 2002. Stochastic gradient boosting. - *Computational Statistics and Data Analysis* 38: 367–378.
- GDAL/OGR contributors 2021. GDAL/OGR geospatial data abstraction software library. - Open Source Geospatial Foundation.
- Good, I. J. 1952. Rational decisions. - *Journal of the Royal Statistical Society. Series B (Methodological)* 14: 107–114.
- Gorelick, N. et al. 2017. Google earth engine: Planetary-scale geospatial analysis for everyone. - *Remote sensing of Environment* 202: 18–27.
- Hijmans, R. J. 2021. Terra: Spatial data analysis.
- Hobbs, R. J. et al. 2009. Novel ecosystems: Implications for conservation and restoration. - *Trends in ecology & evolution* 24: 599–605.
- Johnson, V. S. et al. 2006. The role of spatial and temporal scale in colonization and spread of invasive shrubs in early successional habitats. - *Forest Ecology and Management* 228: 124–134.
- Kauth, R. J. and Thomas, G. S. P. 1976. The tasseled cap - a graphic description of the spectral-temporal development of agricultural crops as seen by landsat. - *Symposium on machine processing of remotely sensed data*

- Ke, G. et al. 2017. LightGBM: A highly efficient gradient boosting decision tree (I Guyon, UV Luxburg, S Bengio, H Wallach, R Fergus, S Vishwanathan, and R Garnett, Eds.). - Advances in neural information processing systems 30
- Kennedy, R. E. et al. 2010. Detecting trends in forest disturbance and recovery using yearly landsat time series: 1. LandTrendr — temporal segmentation algorithms. - Remote Sensing of Environment 114: 2897–2910.
- Kennedy, R. E. et al. 2018. Implementation of the LandTrendr algorithm on google earth engine. - Remote Sensing in press.
- King, D. I. and Schlossberg, S. 2014. Synthesis of the conservation value of the early-successional stage in forests of eastern north america. - Forest Ecology and Management 324: 186–195.
- Kulmatiski, A. et al. 2006. Soil history as a primary control on plant invasion in abandoned agricultural fields. - Journal of Applied ecology 43: 868–876.
- LeCun, Y. et al. 2015. Deep learning. - Nature 521: 436–444.
- Lorimer, C. G. 2001. Historical and ecological roles of disturbance in eastern north american forests: 9,000 years of change. - Wildlife Society Bulletin (1973-2006) 29: 425–439.
- Mahoney, M. J. et al. 2022. terrainr: An R package for creating immersive virtual environments. - Journal of Open Source Software 7: 4060.
- McCay, T. S. and McCay, D. H. 2009. Processes regulating the invasion of european buckthorn (*rhamnus cathartica*) in three habitats of the northeastern united states. - Biological Invasions 11: 1835–1844.
- NOAA National Centers for Environmental Information 2022. Climate at a glance: Statewide mapping.
- Perring, M. P. et al. 2013. Incorporating novelty and novel ecosystems into restoration planning and practice in the 21st century. - Ecological Processes 2: 1–8.
- PRISM Climate Group 2022. PRISM climate data.
- Python Core Team 2022. Python: A dynamic, open source programming language. - Python Software Foundation.
- R Core Team 2021. R: A language and environment for statistical computing. - R Foundation for Statistical Computing.
- Roussel, J.-R. et al. 2020. lidR: An r package for analysis of airborne laser scanning (ALS) data. - Remote Sensing of Environment 251: 112061.
- Ruiz, L. Á. et al. 2018. An object-based approach for mapping forest structural types based on low-density LiDAR and multispectral imagery. - Geocarto International 33: 443–457.
- Spiering, D. J. 2019. Brownfields and old-fields: Vegetation succession in post-industrial ecosystems of western new york.
- Stover, M. E. and Marks, P. 1998. Successional vegetation on abandoned cultivated and pastured land in tomkins county, new york. - Journal of the Torrey Botanical Society: 150–164.
- U.S. Fish and Wildlife Service 2021. National wetlands inventory.
- U.S. Geological Survey 2019. 3D elevation program 1-meter resolution digital elevation model.
- USDA National Agricultural Statistics Service 2019. 2017 census of agriculture.
- Whitney, G. G. 1994. From coastal wilderness to fruited plain: A history of environmental change in temperate north america from 1500 to the present. - Cambridge University Press.
- Wickham, J. et al. 2021. Thematic accuracy assessment of the NLCD 2016 land cover for the conterminous united states. - Remote Sensing of Environment 257: 112357.
- Williams, J. W. and Jackson, S. T. 2007. Novel climates, no-analog communities, and ecological surprises. - Frontiers in Ecology and the Environment 5: 475–482.
- Wolpert, D. H. 1992. Stacked generalization. - Neural Networks 5: 241–259.
- Wright, M. N. and Ziegler, A. 2017. ranger: A fast implementation of random forests for high dimensional data in C++ and R. - Journal of Statistical Software 77: 1–17.
- Yang, L. et al. 2018. A new generation of the united states national land cover database: Requirements, research priorities, design, and implementation strategies. - ISPRS Journal of Photogrammetry and Remote Sensing 146: 108–123.
- Youden, W. J. 1950. Index for rating diagnostic tests. - Cancer 3: 32–35.

# Supplementary Materials

## Contents

<b>Online Resources 1: LiDAR Data Sets</b>	<b>2</b>
<b>Online Resources 2: LT-GEE Parameters</b>	<b>5</b>
<b>Supplementary Materials 3: Model predictors</b>	<b>6</b>
<b>Online Resources 3: Model Hyperparameters</b>	<b>7</b>
<b>Online Resources 4: Component Model Accuracies</b>	<b>8</b>
Random Forest (ranger) . . . . .	8
Stochastic GBM (LightGBM) . . . . .	8
Neural Net (keras) . . . . .	9
<b>References</b>	<b>10</b>

## Online Resources 1: LiDAR Data Sets

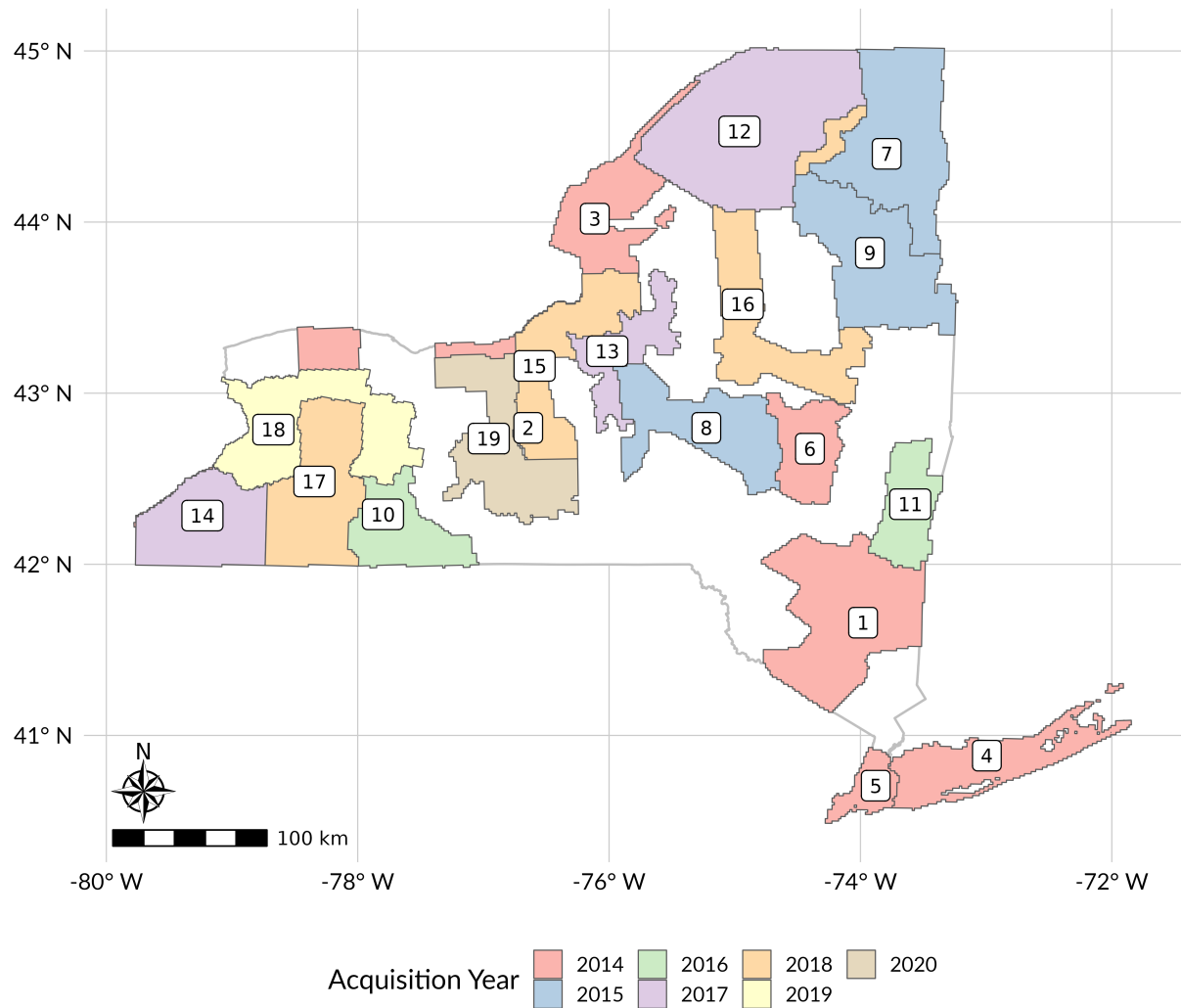


Figure 1: Boundaries for all LiDAR coverages used in this project, colored by year of data acquisition. Numbers on each coverage represent the "index" value of that coverage in table Online Resources 1.

Table 1: Lidar boundaries. "Index" numbers reflect identifier numbers as used in Online Resources Figure 1. Region names reflect the naming conventions used by the NYSGPO; this often, but not always, reflects included counties. Area values are approximate and in square kilometers. Density values are in points per square meter (ppm).

Index	Region Name	Acquisition Year	Area	Density	Citation
1	3 County	2014	7,370	2.04	United States Geological Survey (2015a)
2	Great Gully	2014	720	2.16	Axis GeoSpatial, LLC (2014)
3	Great Lakes	2014	5,780	2.04	United States Geological Survey (2015c)
4	Long Island	2014	3,170	2.04	Woolpert, Inc (2014a)
5	NYC	2014	790	2.04	Woolpert, Inc (2014b)
6	Schoharie	2014	2,500	2.04	United States Geological Survey (2015b)
7	Clinton, Essex & Franklin	2015	1,110	2.04	Quantum Spatial (2016)
8	Madison & Otsego	2015	4,780	2.18	Axis GeoSpatial, LLC (2016a)
9	Warren, Washington & Essex	2015	6,280	3.24	Atlantic Inc (2015)
10	Allegany & Steuben	2016	3,410	2.04	New York Office of Information Technology Services (2016)
11	Columbia & Rensselaer	2016	2,600	2.60	Axis GeoSpatial, LLC (2016b)
12	Franklin & St. Lawrence	2017	9,880	2.04	Quantum Spatial (2017b)
13	Oneida Subbasin	2017	2,550	2.04	Quantum Spatial (2017a)
14	Southwest	2017	4,460	2.04	New York Office of Information Technology Services (2017)
15	Cayuga & Oswego	2018	4,450	2.04	New York Office of Information Technology Services (2018a)

16	Fulton, Saratoga, Herkimer & Franklin	2018	5,010	1.98	Quantum Spatial (2018)
17	Southwest (B)	2018	5,660	2.04	New York Office of Information Technology Services (2018b)
18	Erie, Genesee & Livingston	2019	5,670	2.04	New York Office of Information Technology Services (2019)
19	Central Finger Lakes	2020	5,040	2.04	New York Office of Information Technology Services (2021)

---

## Online Resources 2: LT-GEE Parameters

Table 2: Landtrendr Google Earth Engine (LT-GEE) segmentation parameters for 10 Landsat-derived predictors (Kennedy et al. 2018).

Parameters	Annual Reflectance (NBR, TC*)	Disturbance (YOD, MAG)
maxSegments	5	10
spikeThreshold	0.5	0.9
vertexCountOvershoot	3	3
preventOneYearRecovery	true	true
recoveryThreshold	0.25	0.75
pvalThreshold	0.05	0.05
bestModelProportion	0.75	0.75
minObservationsNeeded	6	6

Table 3: Disturbance predictor (YOD, MAG) parameters in LT-GEE.

Parameter	Value	Operator
Delta	Loss	
Sort	Most recent	
Year	1985-Target year	
Magnitude	50	Greater than
Duration	4	Less than
Pre-disturbance spectral value	300	Greater than
Minimum mapping unit	7	

## Supplementary Materials 3: Model predictors

Table 4: Definitions of predictors used for model fitting.

Predictor	Definition
TCB, TCW, TCG	Tassled cap brightness, wetness, and greenness, with noise removed using LT-GEE
NBR	Normalized burn ratio with noise removed using LT-GEE
MAG, YOD	Magnitude and year of most recent disturbance, as identified using LT-GEE
PRECIP, TMAX, TMIN	30-year normals for precipitation, maximum temperature, and minimum temperature, derived from annual PRISM climate models
ASPECT, ELEVATION, SLOPE, TWI	Aspect, elevation, slope, and topographic wetness index derived from a 30-meter digital elevation model
LCSEC	LCMAP secondary land cover classification

## Online Resources 3: Model Hyperparameters

The random forest was fit using 3,000 trees, each using a random bootstrap sample of 20% of the data, sampled with replacement, a minimum node size of 6 observations, a single random variable per split, and splitting to minimize Gini impurity.

The gradient boosting machine was fit using 2,500 trees, each with unlimited depth, a maximum of 14 leaves, a learning rate of 0.01, a minimum of 10 observations per leaf and 3 observations per bin, an L1 regularization constant of 0 and a L2 regularization constant of 0.5. Each tree was fit using a new bootstrap sample with half the number of observations as the training data, with access to 90% of predictors.

The neural net was a simple additive neural network with seven layers: five densely connected layers with numbers of nodes halving with each additional layer, decreasing from 256 to 128 to 64 to 32 to 16, then feeding into a 20% dropout layer before the final densely connected output layer with a single node. All dense layers used rectified linear activation functions save for the output layer, which used a sigmoid activation function. The model was trained using 1,000 epochs, but final weights used the epoch which maximized the area under the precision-recall curve of the validation data set.

## Online Resources 4: Component Model Accuracies

These tables replicate Table 5 from the manuscript for each of the component models. Metrics reflect equations and definitions from Section 2.4.

### Random Forest (ranger)

Table 5: Model accuracy metrics for the random forest model with predictions classified using various thresholds, calculated using both the balanced test set and the LiDAR patchwork surface. AUC for the LiDAR patchwork was calculated using a random sample of 1,000,000 pixels, while all other metrics used all predicted pixels. Thresholds were selected using a separate validation set, using values chosen to maximize the Youden J statistic ("Youden optimal") or to target a certain minimum specificity ("% specificity").

	Threshold	Sensitivity	Specificity	Precision	F1
<b>Test set (AUC: 0.843)</b>					
Youden optimal	0.519	0.767	0.752	0.754	0.760
90% specificity	0.602	0.537	0.900	0.841	0.655
95% specificity	0.648	0.379	0.951	0.885	0.531
99% specificity	0.704	0.135	0.990	0.930	0.236
<b>LiDAR patchwork (AUC: 0.844)</b>					
Youden optimal	0.519	0.767	0.750	0.075	0.137
90% specificity	0.602	0.533	0.898	0.122	0.199
95% specificity	0.648	0.376	0.950	0.164	0.228
99% specificity	0.704	0.135	0.990	0.253	0.176

### Stochastic GBM (LightGBM)

Table 6: Model accuracy metrics for the gradient boosting machine model with predictions classified using various thresholds, calculated using both the balanced test set and the LiDAR patchwork surface. AUC for the LiDAR patchwork was calculated using a random sample of 1,000,000 pixels, while all other metrics used all predicted pixels. Thresholds were selected using a separate validation set, using values chosen to maximize the Youden J statistic ("Youden optimal") or to target a certain minimum specificity ("% specificity").

	Threshold	Sensitivity	Specificity	Precision	F1
<b>Test set (AUC: 0.889)</b>					
Youden optimal	0.498	0.837	0.776	0.787	0.811
90% specificity	0.699	0.644	0.900	0.864	0.738
95% specificity	0.787	0.485	0.949	0.905	0.632
99% specificity	0.889	0.208	0.990	0.955	0.342
<b>LiDAR patchwork (AUC: 0.890)</b>					
Youden optimal	0.519	0.838	0.773	0.089	0.161
90% specificity	0.602	0.642	0.899	0.144	0.235
95% specificity	0.648	0.482	0.949	0.199	0.282
99% specificity	0.704	0.207	0.990	0.349	0.260

## Neural Net (keras)

Table 7: Model accuracy metrics for the neural net model with predictions classified using various thresholds, calculated using both the balanced test set and the LiDAR patchwork surface. AUC for the LiDAR patchwork was calculated using a random sample of 1,000,000 pixels, while all other metrics used all predicted pixels. Thresholds were selected using a separate validation set, using values chosen to maximize the Youden J statistic ("Youden optimal") or to target a certain minimum specificity ("% specificity").

	Threshold	Sensitivity	Specificity	Precision	F1
<b>Test set (AUC: 0.883)</b>					
Youden optimal	0.494	0.830	0.774	0.784	0.806
90% specificity	0.704	0.618	0.901	0.861	0.720
95% specificity	0.791	0.441	0.950	0.899	0.592
99% specificity	0.886	0.185	0.987	0.942	0.309
<b>LiDAR patchwork (AUC: 0.901)</b>					
Youden optimal	0.519	0.838	0.773	0.089	0.161
90% specificity	0.602	0.642	0.899	0.144	0.235
95% specificity	0.648	0.482	0.949	0.199	0.282
99% specificity	0.704	0.207	0.990	0.349	0.260

## References

- Atlantic Inc 2015. NY\_WarrenWashingtonEssex\_Spring2015.
- Axis GeoSpatial, LLC 2014. 13367 great gully LiDAR.
- Axis GeoSpatial, LLC 2016b. Axis GeoSpatial, LLC new york tiled LiDAR.
- Axis GeoSpatial, LLC 2016a. New york office of information technology services classified LiDAR tiles.
- New York Office of Information Technology Services 2016. Allegany and steuben counties, new york lidar; overall project metadata.
- New York Office of Information Technology Services 2017. Southwest 17 - spring, new york lidar; classified point cloud.
- New York Office of Information Technology Services 2018b. Southwest 17-b - fall, new york lidar; classified point cloud.
- New York Office of Information Technology Services 2018a. LIDAR collection (QL2) for cayuga county and most of oswego county, new york lidar; classified point cloud.
- New York Office of Information Technology Services 2019. LIDAR collection (QL2) for erie, genesee, and livingston counties new york lidar; classified point cloud.
- New York Office of Information Technology Services 2021. Lidar collection (QL2) of all or part of schuyler, seneca, steuben, tomkins, wayne and yates counties, NY lidar; classified point cloud.
- Quantum Spatial 2016. Clinton-essex-lake champlain new york 2015 LiDAR USGS contract: G10PC00026 task order number: G10PC00026 and G14PD000943 (modification) NY\_ClintonEssex\_2015.
- Quantum Spatial, Inc 2017a. New york FEMA 2016 QL2 LiDAR - east zone AOI; classified point cloud.
- Quantum Spatial, Inc 2017b. New york FEMA 2016 QL2 LiDAR - central zone AOI; classified point cloud.
- Quantum Spatial, Inc 2018. Lidar collection (QL2) of all or part of schuyler, seneca, steuben, tomkins, wayne and yates counties, NY lidar; classified point cloud.
- United States Geological Survey 2015a. LAS.
- United States Geological Survey 2015b. LAS extents.
- United States Geological Survey 2015c. LAS.
- Woolpert, Inc 2014a. USGS long island new york sandy lidar classified LAS 1.2.
- Woolpert, Inc 2014b. USGS new york CMGP sandy lidar.